






Cite this: *Mater. Horiz.*, 2024, 11, 5722

Received 28th June 2024,
Accepted 21st August 2024

DOI: 10.1039/d4mh00826j

rsc.li/materials-horizons

Transparent porous films with real refractive index close to unity for photonic applications†

José M. Miranda-Muñoz,‡ José M. Viaña,‡ Mauricio E. Calvo,  Gabriel Lozano * and Hernán Míguez *

Herein, we demonstrate mechanically stable large-area thin films with a purely real refractive index (n) close to 1 in the optical range. At specific wavelengths, it can reach values as small as $n = 1.02$, the lowest reported for thin solid slabs. These are made of a random network of interwoven spherical silica shells, created by chemical vapour deposition of a thin layer of silica on the surface of randomly packed monodisperse polymer nanoparticles that form a film. Thermal processing of the composites results in highly porous silica-based transparent thin films. We demonstrate the potential of this approach by making novel photonic materials such as strong optical diffusers, built by integrating scattering centers within the ultralow n transparent films, or highly efficient light-emitting slabs, in which losses by total internal reflection are practically absent as a result of the almost null optical impedance at the film-air interface.

New concepts

In this manuscript, we demonstrate a new approach to develop highly transparent thin films with effective refractive index close to unity that can be easily generalized to create highly performing photonic materials. Central to the procedure herein proposed is the used of sacrificial polymer nanosphere thin films that can be coated by chemical vapor deposition with thin interconnected shells of metal oxides, which gives rise to ultralow refractive index slabs upon removal of the organic template. The method herein presented is compatible with the processing techniques employed for other nanomaterials, which allows us to overcome the challenge of integrating ultralow refractive index materials into more complex photonic architectures. As proofs-of-principle of their potential significance in the field of photonics, we show how to obtain (i) a very thin film acting as a highly diffusive random optical medium, which results from the high refractive index contrast between the air-like refractive index film and spherical scatterers dispersed in it, and (ii) a film loaded with nanophosphors displaying enhanced photoluminescence out-coupling, as a result of the reduced light guiding losses achieved by the low dielectric contrast between the host of the emitters and the surrounding environment.

Introduction

Solids with low refractive index are central for applications that benefit from high-speed transmission of optical signals, such as optical communications,^{1,2} or that require enhanced radiation coupling from and into free space, as it is the case in photovoltaic³ and light emitting devices,⁴ respectively. Several other phenomena of technological relevance leverage low refractive index materials, such as the total internal reflection in optical fibers,⁵ strong light-matter coupling in quantum dots,⁶ high dielectric contrast in photonic materials,^{7–9} or sensitivity of biosensors,¹⁰ just to name a few. For this reason, the quest for easy-to-process, robust, artificial materials and coatings with near-to-unity index has been a main goal in material science for years.¹¹ In nature, the homogeneous,

dense, solids with the lowest index found, at specific wavelengths, are MgF_2 ($n \approx 1.37$) and SiO_2 ($n \approx 1.45$). One of the most effective and widespread strategies developed to date to further reduce the refractive index of these materials (or of any material, for that matter) consists in increasing their porosity by the introduction of air voids.^{12–14} Aerogels are the archetypical example of this approach.¹⁵ Indeed, aerogels feature an intricate pore network that yield porosity values above 99.9% and a remarkable capacity to be loaded, due to a large specific surface area.^{16,17} At the same time, they are typically bulky, inherently fragile and present a white diffuse reflection as a result of the presence of a large number of disordered sub-micron size air cavities surrounded by a dielectric shell, which gives rise to a large number of air-solid interfaces in which light is scattered.¹⁸ In this regard, significant progress has been made to improve both their mechanical stability and transparency, which has led to application of these materials for glazing in buildings.¹⁹ From a different perspective, thin coatings (*i.e.*, with thickness of \sim a few microns) with a low n have been

Instituto de Ciencias de Materiales de Sevilla (Consejo Superior de Investigaciones Científicas-Universidad de Sevilla), C/Américo Vespucio, 49, Sevilla, 41092, Spain.
E-mail: g.lozano@csic.es, h.miguez@csic.es

† Electronic supplementary information (ESI) available. See DOI: <https://doi.org/10.1039/d4mh00826j>

‡ Equal contribution.



obtained from the deposition of silica nanorods by vacuum-assisted oblique angle deposition^{14–21} or by the integration of hollow nanoparticles, which has turned out to be highly effective to prepare slabs with refractive index slightly below 1.10.^{22–24} Finally, sophisticated methods based on the nano-etching of a mesostructured silica layer or the atomic layer deposition of Al₂O₃ over a sacrificial 3D polymer template defined by nanolithography has yielded films with indices as low as 1.025 in the visible part of the electromagnetic spectrum.^{25,26} However, the integration of these air-like films in actual photonic materials with improved properties is not straightforward and has not been shown yet.

Herein, we present a bottom-up approach to the fabrication of an inexpensive low-refractive-index material in the shape of a film based on a highly porous SiO₂ network, which, as we show, serves as a platform to develop novel multifunctional optical materials. The procedure, consisting of the combination of solution-processing of a sacrificial porous polymer layer and chemical vapour deposition (CVD) of a metal oxide, enables accurate control over the effective refractive index of the eventual film. Coatings (~2 μm thick) prepared by this procedure show a refractive index in the 1.15–1.02 range (at specific wavelengths) and display high average transparency, evidenced by the low degree of diffuse transmittance revealed by the angular distribution of the scattered light. Besides, the versatility of the method proposed is demonstrated by combining it with other materials to build highly efficient thin diffusers and light-emitting coatings with improved outcoupling. In particular, we fabricate an optically disordered medium (specifically, a Mie glass⁹), through the integration of randomly distributed high-refractive-index particles (crystalline TiO₂ spheres in this case), which exhibit an unusually high diffusion strength as a result of the enhanced refractive index contrast between the TiO₂ inclusions and the ultralow refractive index matrix. Thin coatings prepared in this way show a considerable opacity, with scattering mean free path values below 1 μm throughout the visible. To further prove the adaptability of the ultralow *n* material herein proposed, we use it to embed light-emitting Eu³⁺-doped nanoparticles. As a result, the fraction of the photoluminescence that is outcoupled from the emissive coating is 3.4 times larger than that of a reference film of higher refractive index made with the same nanophosphors.

Results and discussion

A bottom-up procedure is devised for the fabrication of ultralow refractive-index films consisting in wide-area, highly porous SiO₂ networks. Full details are provided in the Methods section. In brief, we employ solution-processed films of packed monodisperse polystyrene (PS) nanospheres, which serve as a scaffold for the SiO₂ structure. The latter is grown taking advantage of a chemical vapour deposition procedure originally developed to enhance the mechanical stability and control the filling fraction of artificial opals.²⁷ It consists in the sequential infiltration of reactants in the vapour phase throughout the

voids of the porous polystyrene network to form an extremely thin layer of metal oxide (SiO₂, in our case) on the polymer nanospheres' surface. In the first place, films of PS-spheres with thicknesses up to *ca.* 2 μm are prepared *via* spin-coating, as schematized in Fig. 1(a). Then, films are subsequently placed inside the reactor of a CVD setup in an inert N₂ environment, where they are infiltrated with silicon tetrachloride (SiCl₄) in vapour phase, followed by infiltration with H₂O vapour, thus completing an infiltration cycle, as illustrated in Fig. 1(b). Reaction of the two substances throughout the scaffold leads to the formation of an interconnected network of very thin SiO₂ shells. Further increase of this shell thickness is possible by repeating the metal oxide synthetic cycle, thus allowing the control of the volume filling fraction (*ff*) occupied by SiO₂. Eventually, thermal treatment enables removal of the PS particles yielding a mechanically stable SiO₂ network of very high porosity, as indicated in Fig. 1(c). Please note that the size of the PS beads (168 ± 1 nm diameter) is chosen to prevent potential diffuse scattering by the final SiO₂ network.

The procedure herein presented allows the fabrication of thin films, as displayed in Fig. 2(a), where a scanning electron microscopy (SEM) image of a cross section attained by focused ion beam (FIB) is shown. Higher magnification images, like the one shown in Fig. 2(b), allows to observe with more clarity the random porous network attained. Films with this structure displayed high transparency in the visible range, as shown in Fig. 2(c). By successive CVD infiltration cycles, we obtain films with increasingly higher amounts of infiltrated SiO₂ and hence gradually larger effective refractive index, as this is estimated by averaging the refractive index of its constituents according to a variety of approximations and physical criteria, such as their filling fraction or the way in which they are spatially distributed. The specular reflectance (*R_s*) of these films depends on the refractive index contrast between the film and the medium in which light propagates before reaching the material. Comparison between the measured *R_s* spectra of the films, plotted in Fig. 2(d) along with that of the bare glass substrate (black line), reveals that, in all cases, the porous SiO₂ film acts as an anti-reflective coating, being such behaviour more pronounced as the number of infiltration cycles increases. The effective refractive index of each film is assessed by fitting the experimental *R_s* (dashed gray lines in Fig. 2(d)) employing an approach based on a transfer matrix formalism, fully detailed in the Methods section. Results are shown in Fig. 2(e), confirming that the effective refractive index increases with the number of CVD cycles. Please note that measurements fail to show spectral optical fringes associated to interference of light between reflected and transmitted beams in the low-index film, which we attribute to a certain lack of uniformity across the area probed in the experiments (~1 cm²) caused by thickness variations in the sacrificial latex nanoparticle film. To account for this effect, the simulated *R_s* curves in Fig. 2(d) are obtained after averaging over a certain film thickness range. In spite of this, our method provides reproducible results because the properties are essentially the same when measured at different mm² spots within a given sample and also when compared to other similarly processed samples.



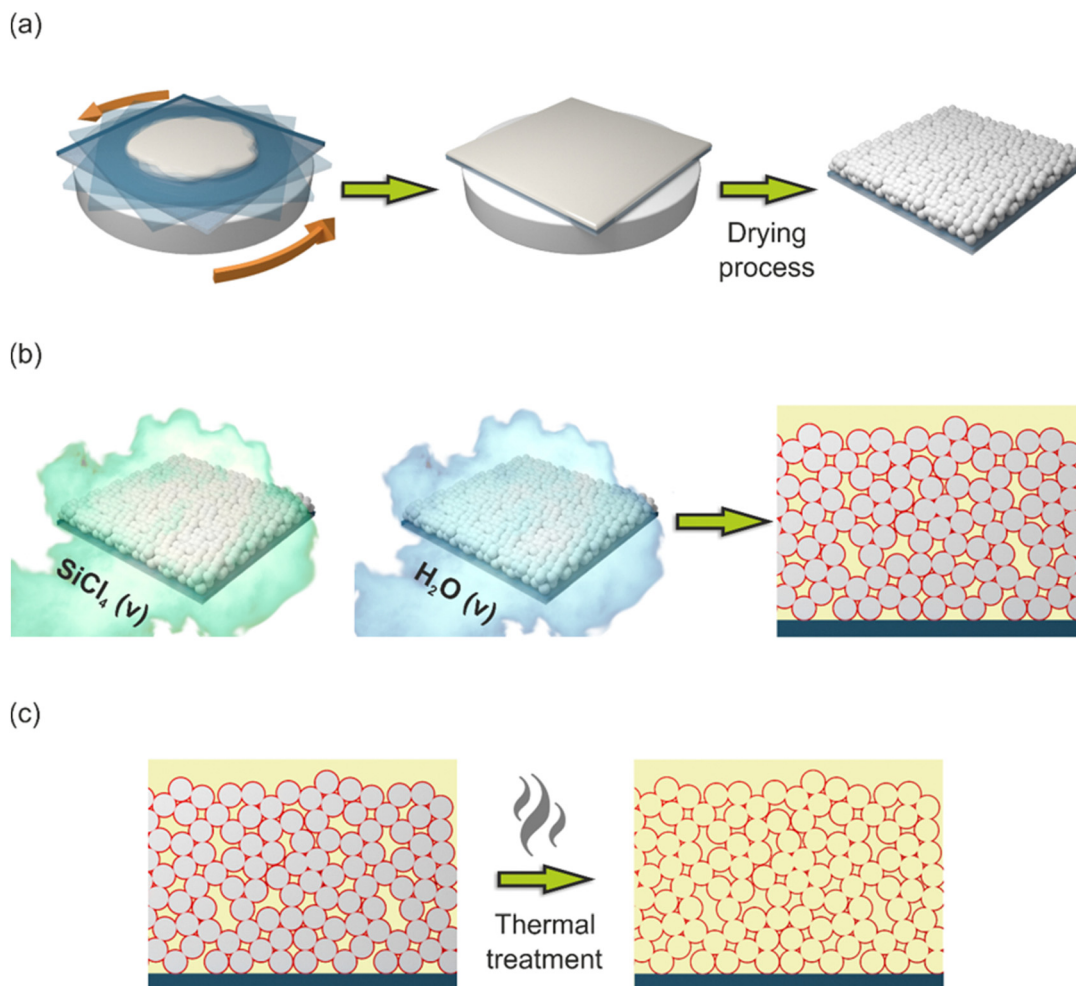


Fig. 1 Schematic description of the fabrication process of a highly porous SiO₂ film from an initial dispersion of PS spheres. (a) Deposition of monodisperse polystyrene nanosphere layer. (b) Precursor infiltration by CVD and formation of a network of SiO₂ shells coating the polystyrene nanospheres. (c) Polystyrene scaffold removal by thermal treatment to achieve the ultralow *n* thin film.

Our results thus prove that, not only the proposed procedure enables the fabrication of films of low refractive index, but it also offers control over it. It is noteworthy that films prepared with one single infiltration cycle yields refractive index values as low as 1.02 at $\lambda = 800$ nm. Such value is to our knowledge amongst the lowest ever reported for a wide-area film. Furthermore, if an effective refractive index of $n_1 = 1.02$ for the film fabricated by means of one infiltration cycle is considered and $n_2 = 1.46$ is taken as the refractive index value of SiO₂, a porosity $p \approx 96\%$ for this ultralow-refractive-index film can be estimated according to the Lorentz–Lorenz expression:

$$p = 1 - \frac{n_1^2 - 1}{n_2^2 - 1} \quad (1)$$

Angular analysis of the scattered light, carried out employing a double goniometer attached to a spectrophotometer, reveal that the amount of both transmitted and reflected diffuse light was negligible, in good agreement with the high transparency observed with the naked eye. In this context, our

group has recently performed a thorough analysis of the optical properties of weakly scattering films made of nanoparticles based on the analysis of the angular distribution of scattered light.²⁸ A similar study for the ultralow refractive index films herein presented is reported in Fig. 2(f). The observed pattern, which shows that all transmitted light is almost perfectly (within a $\pm 5^\circ$ forward cone) ballistically transmitted, confirms that our low-index films, despite their complex internal structure, exhibit hardly any scattering due to the extremely weak index modulation. These measurements are performed by illuminating cm-scale samples over areas of a few mm², emphasizing that our films are definitely homogeneous on a macroscopic scale.

In what follows, we explore the potential of the ultralow *n* films herein presented to serve as the basis to build novel photonic materials. First, we used them to embed aleatorily distributed scattering centres, demonstrating a novel class of Mie glass, an optical random media in which the optical response depends exclusively on the concentration of inclusions and the refractive index contrast between them and the (in this case, ultralow) *n* host matrix. Full details are available in



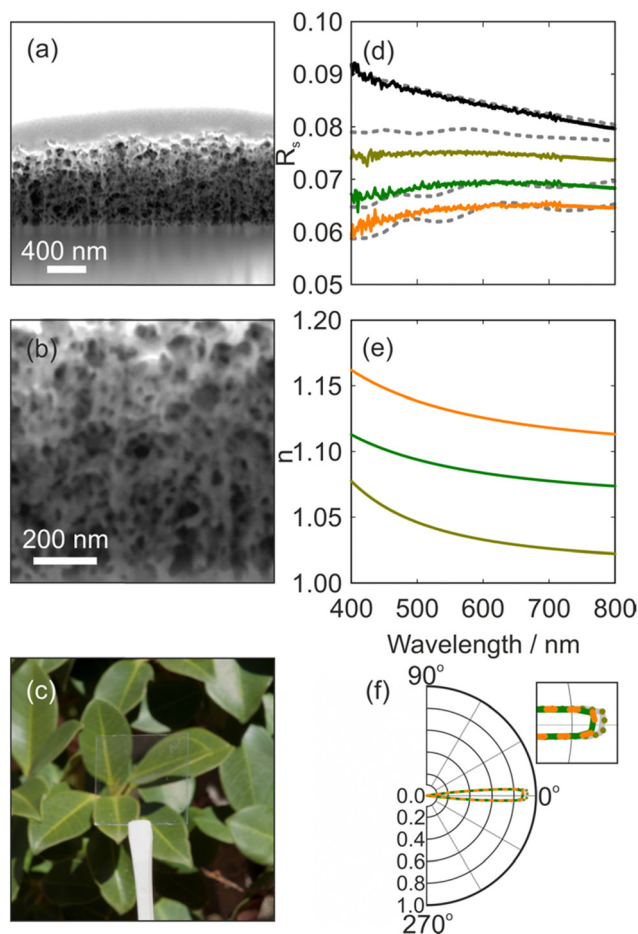


Fig. 2 FIB-SEM cross section images of the structure of an ultralow n porous SiO_2 film, at (a) higher and (b) lower magnifications. (c) Photograph of the ultralow n material, exemplifying its high transparency. (d) Experimental specular reflectance of glass substrates without (gray line) and with an ultralow n porous SiO_2 film deposited on top after 1, 2 and 3 CVD infiltration cycles (olive, green and orange lines, respectively). Dashed lines are the corresponding calculated spectra. (e) Wavelength dependent refractive index for the ultralow n porous SiO_2 films characterized in (d), using the same colour code. (f) Angular distribution of the light scattered by the ultralow n porous SiO_2 films characterized in (e) and (d), using the same colour code.

the Methods section. Specifically, TiO_2 spheres of different sizes are dispersed in a 5% concentration into the ultralow n SiO_2 films. The inclusion of particles with volume filling fraction values above 5% was not feasible, as unwanted inhomogeneities arose for higher scattering centre concentrations, thus preventing the films from displaying both good optical quality and sufficient mechanical stability. The SEM cross-section images in Fig. 3(a) and (b) reveal the random distribution of TiO_2 spheres embedded in the highly porous SiO_2 film. Consequently, intense diffuse light scattering is triggered by the presence of the inclusions, causing both white appearance and significant opacity, as shown in Fig. 3(c). Ballistic transmittance (T_b) spectra were measured and compared to that of the low-refractive-index- SiO_2 film previously characterised, as included in the ESI† (Fig. S1), confirming that, light is

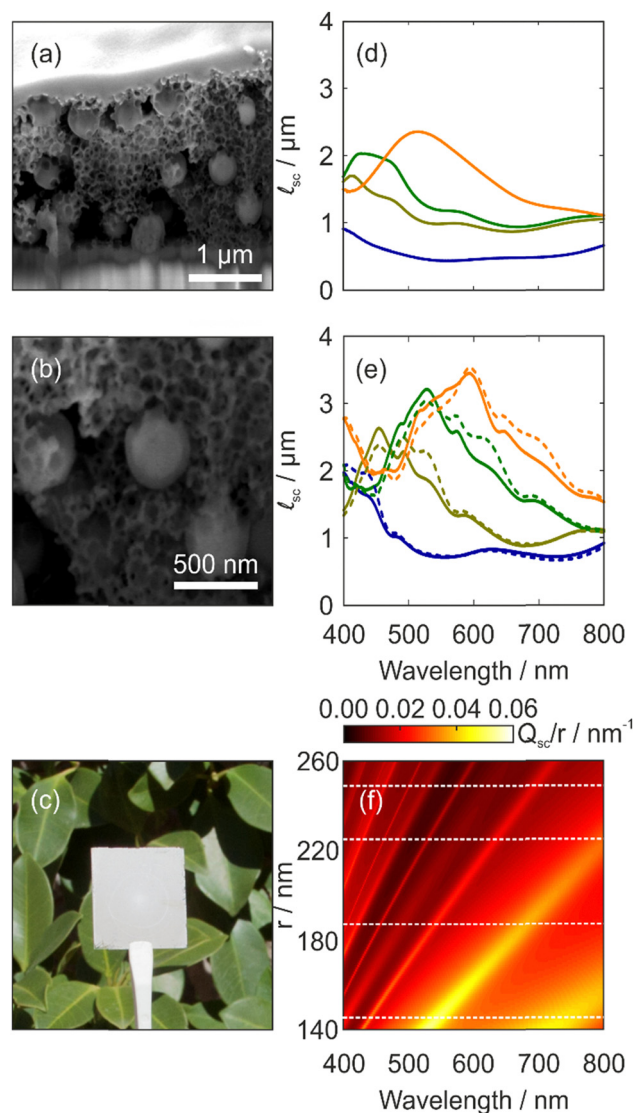


Fig. 3 FIB-SEM cross section images of an ultralow n porous SiO_2 film, at (a) higher and (b) lower magnifications, integrating large spherical TiO_2 scattering centres (radius $r = 225 \pm 20$ nm, $ff = 5\%$). (c) Photograph of a highly porous SiO_2 film integrating TiO_2 scattering centres, evidencing its strongly diffusive character. Spectral scattering mean free path curves extracted from (d) experimental measurements and from (e) calculations for films consisting of an ultralow n porous SiO_2 film embedding large TiO_2 spheres of radii $r = 146 \pm 15$ nm, $r = 188 \pm 15$ nm, $r = 225 \pm 20$ nm and $r = 250 \pm 30$ nm (blue, olive, green and orange lines, respectively, $ff = 5\%$). The dashed lines in (e) are the l_{sc} values calculated for films embedding TiO_2 spheres of similar sizes and concentration randomly dispersed in air. (f) Map of the calculated Q_{sc}/r ratio for spherical TiO_2 spheres embedded in a highly porous SiO_2 matrix versus wavelength and TiO_2 sphere radius. The nominal sizes $r = 146$ nm, $r = 188$ nm, $r = 225$ nm and $r = 250$ nm have been highlighted in white dashed lines.

efficiently scattered and removed from the incident beam, therefore boosting diffuse propagation at the expense of T_b . These observations necessarily imply that the average distance at which photons undergo a scattering event (*i.e.*, the scattering mean free path, l_{sc}) in the TiO_2 sphere loaded ultralow n porous matrix is significantly shorter than the 2 μm thickness of the



films at visible wavelengths. Hence l_{sc} spectra were determined for different sizes of the inclusions from experimental R_s and T_b measurements, according to a procedure already reported.⁹ Fig. 3(d) shows results on high refractive index contrast diffusers based on the inclusion of TiO_2 scattering centers with radii $146 \text{ nm} \pm 15 \text{ nm}$, $188 \text{ nm} \pm 15 \text{ nm}$ and $215 \text{ nm} \pm 20 \text{ nm}$. The high refractive index contrast between the TiO_2 inclusions and the embedding SiO_2 matrix is responsible for l_{sc} values as short as 436 nm at $\lambda = 565 \text{ nm}$ for an inclusion size with $r = (146 \pm 15) \text{ nm}$. These experimental l_{sc} spectra agree well with calculated ones, displayed in Fig. 3(e), which fairly reproduce the trends experimentally observed. However, it is worth mentioning that the reported trend is opposite to previous observations for similar optically disordered materials, where either an increase of the size or the concentration of the scattering centres entailed shorter values of l_{sc} .¹⁹ This can be understood in terms of the ratio between the scattering efficiency, Q_{sc} , and the size of the particle, that is, Q_{sc}/r , which is a consequence of the definition of the scattering mean free path:²⁹

$$l_{sc} = \frac{1}{\rho \sigma_{sc}} \quad (2)$$

Being ρ the particle density number and σ_{sc} the wavelength dependent scattering cross section of the inclusion under consideration, which can be calculated within the Mie formalism for the scattering of light by a small spherical particle.^{30,31} Eqn (2) can be expressed as:

$$l_{sc} = \frac{4}{3f \frac{Q_{sc}}{r}} \quad (3)$$

where f is the volume filling fraction of the inclusions in the porous matrix and Q_{sc} the scattering efficiency, defined as the ratio between the scattering cross section and the geometrical cross section of the particle, $\frac{\sigma_{sc}}{\pi r^2}$ in this case. Fig. 3(f) displays the variation of Q_{sc}/r with the size of the inclusions. As the ratio Q_{sc}/r increases, shorter values of l_{sc} are expected, therefore justifying the trend displayed in Fig. 3(d) and (e), according to which the shortest l_{sc} values are expected for the smallest inclusions we employed. Please note that our calculations assume the scattering centre concentration to be low enough as to allow a description of light scattering in the individual scattering regime according to Mie formalism, *i.e.* accounting only for single-particle scattering effects. Hence, the agreement found confirm that the fabricated films behaved as Mie glasses. Finally, Fig. 3(e) also includes calculated l_{sc} spectra corresponding to a hypothetical system consisting of spherical TiO_2 particles suspended in air (dashed lines). Remarkably, the similarities between these spectra and those determined for the system herein studied evidence the air-like behaviour of our highly porous SiO_2 films. In practical terms, our low-refractive-index- SiO_2 film resembles a layer of air as far as the optical properties are concerned, but its mechanical properties are good enough as to support large inclusions acting as scattering centres.

From a different standpoint, when dealing with photoluminescence colour converting layers, the emission intensity we perceive depends on phenomena occurring at both excitation and emission frequencies. In particular, the external photoluminescence efficiency (EPLE), *e.g.* the fraction of the incident light that reaches our eye after being frequency-converted, can be expressed as the product of three distinct factors: (i) the absorptance (A), *e.g.* the fraction of the incident light absorbed by the material at the excitation wavelength; (ii) the PL quantum yield (PLQY), *e.g.* the fraction of the absorbed light that is down-shifted; and finally (iii) the outcoupling efficiency (χ), *e.g.* the fraction of the generated light that escapes the material in a given solid angle. In general, the higher the refractive index of the material in which light is generated, the lower χ . This represents one of the main challenges of light emitting device (LED) technology since light is typically generated in high-index semiconductors, being a significant fraction of the emission trapped in the material by total internal reflection (TIR) and, thus, lost.³² As a result, state-of-the-art devices include light-management strategies to limit these losses and maximize external efficiency.^{33,34} In this context, we tested our ultralow n films as matrices for light sources, with the aim of studying if the air-like character of the matrix provides a reduction of the losses associated to light guiding inside the film caused by TIR.

As proof of principle, we study the outcoupling efficiency of the photoluminescence (PL) of $\text{GdVO}_4:\text{Eu}^{3+}$ nanophosphors when they are integrated in our low-index SiO_2 matrix. We choose GdVO_4 as a host for the Eu^{3+} active cations because $(\text{VO}_4)^{3-}$ -based matrices enable the efficient excitation of the activators *via* energy transfer. As a result, this nanophosphor is very bright when excited in the UV region of the electromagnetic spectrum, with the most intense emission band in the red. For comparison, we deposit the same nanophosphors over a glass substrate to form an all-nanophosphor film. The fabrication procedure is similar to the one described above, being the only difference the addition of nanophosphors to the initial PS dispersion. Full details are provided in the Methods section. Fig. 4(a) shows a SEM cross section of an intermediate step of the preparation, before removing the PS scaffold, where it can be observed that nanophosphors are randomly distributed in the PS film. Light-emitting films attained are fully transparent, being the fraction of light diffusely scattered at the emission wavelengths below 1%, and feature bright red emission, as illustrated by the picture of the PL displayed in Fig. 4(b). In order to assess the χ enhancement of the nanophosphors in the air-like matrix, we measure the PL spectrum under UV excitation ($\lambda = 276 \text{ nm}$) and normalize it by $A = 0.13$ and $\text{PLQY} = 0.19$. For comparison, we also measure the PL of the reference film and correct it following a similar procedure, being in this case $A = 0.59$ and $\text{PLQY} = 0.48$. Notice that A of the air-like emitting film is smaller than that of the reference due to the larger amount of nanophosphors in the reference film. Also, we attain smaller values of PLQY for the nanophosphors embedded in the low-index film. We attribute this to a two different factors. First, the air-like matrix provides a significant reduction in the radiative decay rate (Γ_r) of the Eu^{3+} transition due to the much



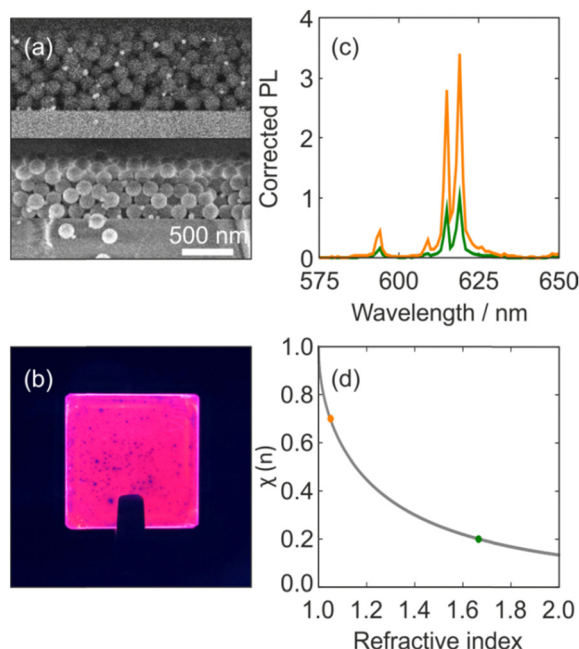


Fig. 4 (a) Back scattered (top) and secondary electron (bottom) SEM micrographs of a cross section of a polystyrene sphere layer embedded with $\text{VO}_4\text{Gd:Eu}^{3+}$ nanophosphors (identified as bright dots in the top image). (b) Photograph of the glow of an ultralow n film embedded with nanophosphors under UV excitation. (c) PL spectra of a reference $\text{VO}_4\text{Gd:Eu}^{3+}$ nanophosphor layer (green line) and of an ultralow n film containing similar luminescent nanoparticles (orange line), corrected by the ratio of the absorbance of the excitation wavelength and the PL quantum yield in each case, for the sake of comparison. (d) Theoretical outcoupling efficiency, χ , vs. n , as given by eqn (5). The observed χ values for the reference ($n = 1.67$) and an ultralow n ($n = 1.05$) film containing a 5% nanophosphor ff are indicated with green and orange spots, respectively.

lower refractive index of the effective medium in which cations are embedded. In fact, according to a simple nanocrystal cavity model,^{35,36}

$$\Gamma_{\text{r}}(n_1) = \Gamma_0 n_1 \left(\frac{3n_1^2}{2n_1^2 + n_{\text{NC}}^2} \right)^2 \quad (4)$$

with Γ_0 the radiative decay in vacuum, and n_{NC} the index of the nanocrystals (≈ 2.1), a ~ 4 -fold reduction is expected for nanocrystals embedded in a 1.05 effective index layer. On the other hand, there are subtle differences in the processing of the nanophosphors. Indeed, although we subjected both samples to the same annealing temperature, differences in the CVD of the SiO_2 may affect the surface chemistry of the nanophosphors, which may result in different non-radiative decay pathways that impact on the efficiency. Fig. 4(c) shows the corrected PL spectra of both samples normalized to the maximum of the PL of the reference film, which allows to estimate χ enhancement (non-corrected A and PL spectra of all samples under analysis can be seen in Fig. S2 (ESI[†]), as well as the time resolved PL analysis in Fig. S3 and Table S1, ESI[†]). Two emission bands are clearly observed at ~ 580 nm and ~ 615 nm, which are associated to Eu^{3+} transitions from $^5\text{D}_0$ to $^7\text{F}_1$ and $^7\text{F}_2$, respectively. Our results indicate that the emission of nanophosphors in an air-like matrix

is outcoupled ~ 3.5 times more efficiently than that of the same nanophosphors packed in a reference film. Most generated light does not suffer from TIR trapping, as indicated by the low fraction of the emitted light that escapes through the edges of the sample – see Fig. 4(b). Indeed, it is possible to estimate χ as a function of the refractive index of the film from which light is emitted (n_1), according to:²⁴

$$\chi = 1 - \left(1 - \frac{1}{n_1^2} \right)^{1/2} \quad (5)$$

We plot χ versus the effective refractive index of the layer in Fig. 4(d). In particular, according to the estimation of the effective refractive index of the air-like film loaded with nanophosphors ($n = 1.05$ at $\lambda = 619$ nm), we extract $\chi = 0.70$. A 3.5 reduction in χ would be associated to an effective refractive index of 1.67, which agrees well with the value expected for the reference nanophosphor layer. Fig. 4(d) also includes the (n, χ) coordinates associated to air-like and reference films. Our results demonstrate that a low refractive index matrix boosts the light-extraction efficiency of light sources embedded within, which could be of direct application in the development of novel color converting layers. Our results also reveal a trade-off between PLQY, which decreases with the refractive index of the embedding matrix, and outcoupling efficiency, which follows the opposite trend, that deserves attention in the design and optimization of color conversion devices. It should be noted that in order to adapt our approach to electroluminescent materials further research will be needed to allow charge injection in the said matrix.

Finally, to better put into context the results herein presented, in Table 1 we provide a list of low refractive index materials reported up to date and a summary of their most relevant properties.

Conclusions

In conclusion, we have demonstrated mechanically stable thin films with a refractive index close to one, which serve as versatile platform to develop effective diffusers and light-emitting coatings featuring large out-coupling efficiency. A highly porous silica network is obtained as a result of the chemical vapour deposition of a thin layer of silica over a random packing of polymer nanobeads employed as sacrificial scaffold. Resulting films are transparent and feature values of the effective refractive index, which can be accurately controlled between 1.02 and 1.15 depending on the silica deposition process. Taking advantage of the low value of the refractive index of the matrix, we prove an optically random material integrating TiO_2 spheres, which behave as a Mie diffuser. The large refractive index contrast between the scattering centers and the air-like matrix allows demonstrating materials with values of the scattering mean free paths below $1 \mu\text{m}$ in a broad spectral range. Also, we use our air-like matrix to embed light-emitting nanophosphors to show light-emitting coatings with a light-extraction efficiency of 70%, which is 3.5 times larger than



Table 1 List various low refractive index materials reported to date and summary of their main optical properties

Composition	Processing method	Thin Film	Index value	Transparency	Photolum.	Ref.
PMMA/PS	Nanophase separation of polymers	Yes (70–200 nm)	1.05–1.2	91–99%	No	37
SiO ₂	Nano-rod films by oblique angle deposition	Yes (1.35 μ m)	1.08	Not reported	No	20
SiO ₂	Nano-rod films by oblique angle deposition	Yes (482 nm)	1.054 at 620 nm	Not reported	No	11
SiO ₂	Nano-rod films by oblique angle deposition	Yes (25–225 nm)	1.05–1.46 at 632 nm	Not reported	No	21
Magnesium oxyfluoride	Liquid processing and rapid annealing	Yes (320–430 nm)	1.09 at 700 nm	Not reported	No	22
SiO ₂	Polymer nanoparticle film as sacrificial template	Yes (100–400 nm)	1.15–1.40 at 600 nm	Not reported	No	13
SiO ₂	Etching of mesoporous silica films	Yes	1.03 at 800 nm	Not reported	No	25
SiO ₂	Sol–gel	Yes	1.10–1.21 at 600 nm	98% at 600 nm	No	24
Al ₂ O ₃	Nanolithography and atomic layer deposition	Yes	1.025–1.36	90% at 800 nm	No	26
SiO ₂	Aerogel	No	1.08 at 633 nm	Not reported	No	6
SiO ₂	Nanoparticle wet deposition	Yes (100 nm)	1.07–1.17	99.9% at 560 nm	No	23
SiO ₂	Ag nanowire array as sacrificial template	Yes (95–155 nm)	1.24–1.36 at 600 nm	Not reported	No	14
Silanized cellulose	Aerogel	No (1–2.5 mm)	1.0025 at 632 nm	97–99%	No	19
SiO ₂	CVD infiltration of a polymer sacrificial film	Yes (100 nm–2 μ m)	1.02 at 800 nm	92–94%	Yes	This work

that of a reference photoluminescence film made of a random packing of the same nanophosphors. Our results illustrate the potential of low-refractive-index materials to develop complex photonic structures of improved properties.

Methods

Fabrication

Ultralow-refractive-index film. A combined procedure comprising solution processing techniques and a step of chemical vapour deposition was employed for the fabrication of films of an ultralow refractive index based on highly porous SiO₂. Specifically, a film consisting of PS spheres served as a scaffold for the subsequent formation of the SiO₂ structure through a previously reported CVD technique.²⁷ In the first place, a suspension of PS spheres of diameter $d = (168 \pm 1)$ nm (IKERLAT Polymers S. L.©) in a mixture of water and absolute ethanol, PS:H₂O:EtOH, was prepared in the proportion 10:45:45 (v/v/v). With that purpose, 20 ml of a 10 vol% commercial suspension of spherical PS particles were centrifuged at 24 000 rpm for 40 minutes, followed by solvent removal. After that, 9 ml of absolute ethanol and 9 ml of Milli-Q water were added to the PS and subjected to a sonication process in order to redisperse the PS spheres. For the fabrication of the PS-sphere-based films, one or two depositions of 200 μ l of the suspension were spun upon a square glass substrate at rotation speed values ranging from 1000 to 4000 rpm for 40 seconds, performing a drying process at 60 °C during 10 minutes in-between depositions. The rotation speed in combination with the number of depositions dictated the thickness of the eventual film. The samples were left to dry overnight at 60 °C. Subsequently, the films were subjected to a CVD process by means of a homemade setup. They were placed in a sealed reactor containing a N₂ atmosphere, where they were subjected to a different number of infiltration cycles, each one consisting in a 1-minute infiltration step with SiCl₄ in vapour phase, followed by a 1-minute infiltration step with H₂O, also in vapour phase. In this way, the SiCl₄ adsorbed to the PS spheres in the

pores among them throughout the whole structure reacted with the H₂O vapour, triggering the formation of SiO₂ partially filling such pores.²⁷ The vapour was generated by bubbling either of both reactants with pressurised N₂, creating a flux into the reactor. Eventually, the films were heated up to 500 °C for 2 hours in order to remove the PS scaffold, thus resulting a highly porous SiO₂ film of thicknesses up to *ca.* 1.5 μ m.

Diffuser. The procedure allowed the inclusion of larger nanocrystalline TiO₂ spheres acting as scattering centres in the film by adding them to the initial PS-sphere suspension. The amount of added TiO₂ particles in relation to the volume of PS spheres defined the volume filling fraction value of TiO₂ scattering centres in the eventual film. Amorphous TiO₂ spheres of diverse sizes for use as scattering centres were synthesised according to a procedure reported elsewhere.³⁸

Emitter. The procedure allowed the inclusion of GdVO₄:Eu³⁺ nanophosphors as light sources in the film by adding them to the initial PS-sphere suspension. The amount of added nanophosphors is 3 vol% in relation to the volume of PS spheres. Amorphous GdVO₄:Eu³⁺ nanophosphors with a size of ~ 40 nm for use as light sources were synthesised according to a procedure reported elsewhere.³⁹

Characterization

Structural characterization. The resulting structure of the films was inspected by means of scanning electron microscopy (SEM) and a SEM microscope combined with a focused ion beam (FIB). The thicknesses of the films were determined from cross-section images generated with a Hitachi S4800 microscope. The cross-section images displayed in the figures of the manuscript were obtained by means of a dual-beam Auriga FIB-SEM equipment (ZEISS®), which uses a focused beam of gallium ions for controlled etching of the sample and subsequent inspection with an SEM microscope.

Optical characterization. The determination of the magnitudes required for the optical characterization depicted in the manuscript was performed through an UV-Vis-NIR spectrophotometer (Cary 5000, Agilent Technologies©) coupled to



the Universal Measurement Accessory (UMA), which enabled the spectral collection of light from any position in a plane perpendicular to the sample at a fixed distance from it (angular distribution measurements) for any angle of the sample holder. Furthermore, the polarisation state of the incident light could be selected. For the extraction of the spectral refractive index of the porous SiO₂ films, measurements of R_s and T_b were performed for three different incidence angles, namely, 6°, 30° and 50°, and both polarisation states. Measurements of R_s and T_b allowed the determination of the l_{sc} of the films integrating optical disorder by means of a procedure already reported.¹⁸

Photoluminescent characterization. Emission spectra and time-dependent PL intensity were measured with an Edinburgh FLS1000 spectrofluorometer under an excitation of $\lambda_{ex} = 276$ nm. Time-dependent PL measurements were registered for the most intense Eu³⁺ emission band at 619 nm. Absolute PLQY measurements were performed in an integrating sphere using FLS1000. Our films were excited at 285 nm, and the emission and scattering peaks measured in the integrating sphere in the spectral range comprised between 270 and 850 nm.

Calculations

Scattering mean free path and scattering cross section. Mie formalism for the scattering of light by a spherical particle was employed for the calculation of the spectral l_{sc} and Q_{sc} .^{30,31}

Reflectance and transmittance. For the calculation of the R_s and T_b spectra, the transfer-matrix method was employed, which allows the determination of the polarisation-dependent R_s and T_b as a function of angle and wavelength of a multilayer system devoid of scattering providing the complex refractive index of each layer and their thickness as input parameters.

Refractive index extraction. The complex refractive indices of the highly porous-SiO₂ films were extracted by fitting the R_s and T_b measurements of the transparent films at three different incidence angles and both polarisation states to the spectra derived from the transfer-matrix method through a genetic algorithm, designed to find the complex refractive index spectra of the film under consideration yielding the best fitting according to a defined model. In this work, the Cauchy Absorbing model was considered.

Angle-dependent scattering calculation. The angular patterns described by the light emerging from the films were simulated according to an upgraded version of a theoretical method previously reported.⁴⁰ The model consists in a combination of a Monte Carlo approach and Mie theory that enables tracing of the trajectory of a photon entering any multilayer system with any number of components in each layer, while taking into account any possible fate of the photon, *i.e.* transmission, reflection, absorption or scattering. When extended to a larger number of photons, the model allows the generation of the spectra derived from the collection of the emergent photons at different angles, such as total and specular reflectance, total and ballistic transmission and their respective diffuse components. Owing to the tracing nature of the model, the extraction of the absorption profiles at each of the layers is possible. Moreover, since information regarding the exit angle of the

photons and the number of scattering events undergone before emerging from the system is available, the model enables the generation of the angular patterns described by the light exiting the film.

Author contributions

HM develop the concept of preparing near unity refractive films by CVD infiltration of sacrificial polymer layers, and co-supervise the research work along with GL. MEC and GL were in charge of devising the synthetic and optical characterization methods, respectively. Most laboratory work was carried out by JMM, who focus on the development and analysis of optical random media, and JMV, whose target was to achieve enhanced outcoupling in color converting layers. Both JMM and JMV equally contributed to this work.

Data availability

The data underlying this study are openly available in the Digital CSIC repository: <https://doi.org/10.20350/digitalCSIC/16528>. The codes used to calculate the scattering mean free path are provided at <https://github.com/Multifunctional-Optical-Materials-Group>.

Conflicts of interest

The authors declare no competing financial interest.

Acknowledgements

This project received funding from the Research State Agency of the Spanish Ministry of Science and Innovation under grant PID2020-116593RB-I00, funded by MCIN/AEI/10.13039/501100011033, the Junta de Andalucía under grant P18-RT-2291 (FEDER/UE), and the European Research Council (ERC) under the European Union's Horizon 2020 Research and Innovation Programme (NANOPHOM, grant agreement no. 715832).

References

- 1 Z. Yu, X. Xi, J. Ma, H. K. Tsang, C. L. Zou and X. Sun, Photonic integrated circuits with bound states in the continuum, *Optica*, 2019, **6**, 1342.
- 2 Y. Koike, T. Ishigure and E. Nihei, High-bandwidth graded-index polymer optical fiber, *J. Light Technol.*, 1995, **13**, 1475.
- 3 S. Liu, Y. Qian, Y. Lin, L. Sun, Y. Zhu and D. Li, Multilayer anti-reflective coating with ultra-low refractive index SiO₂ nanopillars for high efficiency multi-junction GaAs solar cells, *Sol. Energy Mater. Sol. Cells*, 2024, **266**, 112679.
- 4 H. Shin, J. H. Lee, C. K. Moon, J. S. Huh, B. Sim and J. J. Kim, Sky-Blue Phosphorescent OLEDs with 34.1% External Quantum Efficiency Using a Low Refractive Index Electron Transporting Layer, *Adv. Mater.*, 2016, **28**, 4920.



- 5 B. H. Liu, H. Zhu, D. H. Zhao, G. D. Nian, S. X. Qu and W. Yang, Hydrogel Coating Enabling Mechanically Friendly, Step-Index, Functionalized Optical Fiber, *Adv. Opt. Mater.*, 2021, **9**, 2101036.
- 6 X. Jin, Strong coupling of single quantum dots with low-refractive-index/high-refractive-index materials at room temperature, *Sci. Adv.*, 2020, **6**, eabb3095.
- 7 B. Brudieu, A. L. Bris, J. Teisseire, F. Guillemot, G. Dantelle, S. Misra, P. Roca, I. Cabarrocas, F. Sorin and T. Gacoin, Sol-Gel Route Toward Efficient and Robust Distributed Bragg Reflectors for Light Management Applications, *Adv. Opt. Mater.*, 2014, **2**, 1105.
- 8 J.-Q. Xi, J. K. Kim, E. F. Schubert, D. Ye, T.-M. Lu, S.-Y. Lin and J. S. Juneja, Very low-refractive-index optical thin films consisting of an array of SiO₂ nanorods, *Opt. Lett.*, 2006, **31**, 601.
- 9 J. M. Miranda-Muñoz, G. Lozano and H. Míguez, Design and Realization of a Novel Optically Disordered Material: A Demonstration of a Mie Glass, *Adv. Opt. Mater.*, 2017, **5**, 1700025.
- 10 J. Memisevic, V. Korampally, S. Gangopadhyay and S. A. Grant, Characterization of a novel ultra-low refractive index material for biosensor application, *Sens. Actuators, B*, 2009, **141**, 227.
- 11 E. F. Schubert, J. K. Kim and J.-Q. Xi, Low-refractive-index materials: A new class of optical thin-film materials, *Phys. Stat. Sol.*, 2007, **8**, 244.
- 12 J. L. Plawsky, J. K. Kim and E. F. Schubert, Engineered nanoporous and nanostructured films, *Mater. Today*, 2009, **12**, 36.
- 13 F. Guillemot, A. Brunet-Bruneau, E. Bourgeat-Lami, T. Gacoin, E. Barthel and J.-P. Boilot, Latex-templated silica films: tailoring porosity to get a stable low-refractive index, *Chem. Mater.*, 2010, **22**(9), 2822–2828.
- 14 W. Wang, J. Gao, H. Hu, Y. Jiang, H. Wu, X. Li, X. Li, L. Liang, H. Zhang and H. Cao, Air Nanocolumn-SiO₂ composite film with adjustable anisotropic refractive index, *Mater. Today Phys.*, 2022, **26**, 100722.
- 15 C. Ziegler, A. Wolf, W. Liu, A.-K. Herrmann, N. Gaponik and A. Eychmüller, Modern Inorganic Aerogels, *Angew. Chem., Int. Ed.*, 2017, **56**, 43.
- 16 Y. Kim, S. Baek, P. Gupta, C. Kim, K. Chang, S.-P. Ryu, H. Kang, W. S. Kim, J. Muoung, W. Park and K. Kim, Air-like plasmonics with ultralow-refractive-index silica aerogels, *Sci. Rep.*, 2019, **9**, 2265.
- 17 A. Eychmüller, Nanoparticle-Based Aerogels and Their Prospective Future Applications, *J. Phys. Chem. C*, 2022, **126**(45), 19011.
- 18 J. M. Schultz, K. I. Jensen and F. H. Kristiansen, Super insulating aerogel glazing, *Sol. Energy Mater. Sol. Cells*, 2005, **89**, 275.
- 19 E. Abraham, V. Cherpak and B. Senyuk, *et al.*, Highly transparent silanized cellulose aerogels for boosting energy efficiency of glazing in buildings, *Nat. Energy*, 2023, **8**, 381.
- 20 J.-Q. Xi, J. K. Kim and E. F. Schubert, Silica nanorod-array films with very low refractive indices., *Nano Lett.*, 2005, **5**(7), 1385–1387.
- 21 J.-Q. Xi, M. F. Schubert, J. K. Kim, E. F. Schubert, M. Chen, S.-Y. Lin, W. Liu and J. A. Smart, Optical thin-film materials with low refractive index for broadband elimination of Fresnel reflection, *Nat. Photonics*, 2007, **1**, 176.
- 22 D. Grosso, C. Boissière and C. Sanchez, Ultralow-dielectric-constant optical thin films built from magnesium oxyfluoride vesicle-like hollow nanoparticles, *Nat. Mater.*, 2007, **6**, 572–575.
- 23 F. Chi, Y. Zeng, C. Liu, D. Liang, Y. Li, R. Xie, N. Pan and C. Ding, Aggregation of Silica Nanoparticles in Sol-Gel Processes to Create Optical Coatings with Controllable Ultralow Refractive Indices, *ACS Appl. Mater. Interfaces*, 2020, **12**, 16887.
- 24 Y. Zhang, C. Zhao, P. Wang, L. Ye, J. Luo and B. Jiang, A convenient sol-gel approach to the preparation of nanoporous silica coatings with very low refractive indices, *Chem. Commun.*, 2014, **50**, 13813.
- 25 F. Chi, L. Yan, H. Yan, B. Jiang, H. Lv and X. Yuan, Ultralow-refractive-index optical thin films through nanoscale etching of ordered mesoporous silica films, *Opt. Lett.*, 2012, **37**, 9.
- 26 X. A. Zhang, A. Bagal, E. C. Dandley, J. Zhao, C. J. Oldham, B.-I. Wu, G. N. Parsons and C.-H. Chang, Ordered 3D Thin-Shell Nanolattice Materials with Near-Unity Refractive Indices, *Adv. Funct. Mater.*, 2015, **25**, 6644.
- 27 H. Míguez, N. Tétéreault, B. Hatton, S. M. Yang, D. Perovic and G. A. Ozin, Mechanical stability enhancement by pore size and connectivity control in colloidal crystals by layer-by-layer growth of oxide, *Chem. Commun.*, 2002, 2763.
- 28 A. Jiménez-Solano, J. M. Miranda-Muñoz, S. Carretero-Palacios and H. Míguez, Modeling Weakly Scattering Random Media: A Tool to Resolve the Internal Structure of Nanoporous Materials, *Adv. Photonics Res.*, 2023, 2200267.
- 29 P. D. Kaplan, A. D. Dinsmore and A. G. Yodh, Diffuse-transmission spectroscopy: A structural probe of opaque colloidal mixtures, *Phys. Rev. E*, 1994, **50**, 4827.
- 30 G. Mie, Beiträge zur Optik trüber Medien, speziell kolloidaler Metallösungen (Contributions to the optics of cloudy media, especially colloidal metal solutions), *Ann. Phys.*, 1908, **330**, 377.
- 31 C. F. Bohren and D. R. Huffman, *Absorption and Scattering of Light by Small Particles*, John Wiley & Sons, USA, 1983.
- 32 W. Brütting, J. Frischeisen, T. D. Schmidt, B. J. Scholz and C. Mayr, Device efficiency of organic light-emitting diodes: Progress by improved light outcoupling, *Phys. Status Solidi A*, 2013, **210**(1), 44.
- 33 T. Tsutsui, M. Yahiro, H. Yokogawa, K. Kawano and M. Yokoyama, Doubling Coupling-Out Efficiency in Organic Light-Emitting Devices Using a Thin Silica Aerogel Layer, *Adv. Mater.*, 2001, **13**, 15.
- 34 Y. Sun and S. R. Forrest, Enhanced light out-coupling of organic light-emitting devices using embedded low-index grids, *Nat. Photonics*, 2008, **2**, 483.
- 35 T. Senden, F. T. Rabouw and A. Meijerink, Photonic Effects on the Radiative Decay Rate and Luminescence Quantum Yield of Doped Nanocrystals, *ACS Nano*, 2015, **9**, 2.
- 36 M. Romero, J. R. Sánchez-Valencia, G. Lozano and H. Míguez, Effect of the effective refractive index on the radiative decay rate in nanoparticle thin films, *Nanoscale*, 2023, **15**, 15279.



- 37 S. Walheim, E. Schäffer, J. Mlynek and U. Steiner, Nanophase-Separated Polymer Films as High-Performance Antireflection Coatings, *Science*, 1999, **283**, 520.
- 38 Y. J. Kim, M. H. Lee, H. J. Kim, G. Lim, Y. S. Choi, N. Park, K. Kim and W. I. Lee, Formation of Highly Efficient Dye-Sensitized Solar Cells by Hierarchical Pore Generation with Nanoporous TiO₂ Spheres, *Adv. Mater.*, 2009, **21**, 3668.
- 39 N. O. Nuñez, S. Rivera, D. Alcantara, J. M. de la Fuente, J. Garcia-Sevillano and M. Ocaña, Surface modified Eu:GdVO₄ nanocrystals for optical and MRI imaging, *Dalton Trans.*, 2013, **42**, 10725.
- 40 E. Gálvez, P. R. F. Barnes, J. Halme and H. Míguez, Dye sensitized solar cells as optically random photovoltaic media, *Energy Environ. Sci.*, 2014, **7**, 689.

